Analysis and Active Damping of Multiple High Frequency Resonances in DFIG System

Song, Yipeng; Blaabjerg, Frede; Wang, Xiongfei

Published in:
I E E E Transactions on Energy Conversion

DOI (link to publication from Publisher):
10.1109/TEC.2016.2629088

Publication date:
2017

Document Version
Accepted author manuscript, peer reviewed version

Analysis and Active Damping of Multiple High Frequency Resonances in DFIG System

Yipeng Song, *Member, IEEE*, Frede Blaabjerg, *Fellow, IEEE*, Xiongfei Wang, *Member, IEEE*

***Abstract* — As the wind power generation develops, the Doubly Fed Induction Generator (DFIG) based wind power system are more and more likely to operate in the emerging weak network rather than the conventional stiff network. Due to the comparatively large impedance of the weak network than the stiff grid, the DFIG system may be subject to the resonances due to the impedance interaction between the DFIG system and the weak network. Especially, when connected to a series π sections weak network, the Multiple High Frequency Resonances (MHFR) may occur and require careful studies. The impedance modeling of the DFIG system and the series π sections weak network is firstly demonstrated in this paper. Then, due to the multiple magnitude peaks of the series π sections of the weak network, the MHFR will be produced and can be theoretically explained based on the impedance modeling results. For the purpose of mitigating the MHFR, an active damping strategy which introduces a virtual impedance, including a phase leading compensation unit and a virtual positive resistance, is proposed and demonstrated. Simulations are conducted to validate the DFIG system MHFR as well as the proposed active damping strategy.**

***Index Terms* — DFIG system; series π sections weak network; multiple high frequency resonances; virtual impedance; active damping.**

I. Introduction

Due to the continuously increasing demand for the renewable energy within the entire world, the wind power generation has experienced fast growth during the past few decades. The Doubly Fed Induction Generator (DFIG) based wind power system is a popular commercial wind power solution implemented around globe [1]-[3].

As the distributed generation develops fast, the increasing capacity of wind power generation has been achieved by connecting more and more DFIG based wind turbine systems to offshore and distributed networks [4]-[8]. These types of networks are typically smaller scale weak networks with comparatively large network impedances compared to the stiff grid network. As a consequence, the impedance interaction between the weak network and the DFIG system can no longer be neglected, but requires serious attention. There are mainly two kinds of resonances in the DFIG system when connected to the weak network, i.e., the Sub- Synchronous Resonance (SSR) in the case of the series compensated weak network [9]-[15]; the High Frequency Resonance (HFR) in the case of the parallel compensated weak network [16]-[18].

As it has been well analyzed in previous studies [9]-[15], in order to improve the transmission capability of the long distance cables, the series capacitance is employed to reduce the electric length of the long-distance transmission line. However, SSR can unfortunately be produced, and it is pointed out that the impedance interaction between the DFIG system and the series compensated grid network is the direct cause of the SSR [9]-[15]. In order to conduct the theoretical analysis of the SSR, the DFIG system impedance modeling needs to be established as an analysis platform. Refs. [9]-[11] developed the DFIG system positive and negative impedance modeling by the harmonic linearization method. The influences of the rotor current control, phase locked loop control and the various rotor speeds are also investigated. The impedance modeling of the entire DFIG system and the series compensated weak grid network are also reported in [12], with the conclusion that the interaction between the electric network and the converter controller is the main contribution of the SSR phenomena.

As to the active damping of SSR, a virtual resistance is inserted to achieve damping of the DFIG SSR in [9], but yet no theoretical analysis and design procedure of this virtual resistance is reported in details. Similarly, the design of an auxiliary SSR damping controller and the selection of the control signals in the DFIG converters are reported in [15], and several alternative active damping control variables are discussed. In contrast, instead of reshaping the impedance of the DFIG system, a Thyristor- Controlled Series Capacitor (TCSC) – based method is developed [13] to flexibly adjust the series compensated capacitance and then the potential SSR can be avoided.

On the other hand, besides the series compensated weak network, the DFIG system is also likely to be connected to the parallel compensated weak network. As it is discussed in [16]-[18], the High Frequency Resonance (HFR) can be a consequence of the impedance interaction between the DFIG system and the parallel compensated weak network. The frequency of the HFR is estimated based on the Bode diagram of the DFIG system impedance and the parallel compensated weak network impedance in [16]-[18]. Then, the HFR can be mitigated by introducing a virtual impedance to appropriately reshape the DFIG system impedance in order to reduce the phase difference to smaller than 180° and then the HFR can be eliminated [16].

The instability phenomenon is also likely to occur in the grid connected converter [19]-[27] when connected to a

The authors are with the Department of Energy Technology, Aalborg University, Aalborg 9220, Denmark. (e-mail: yis@et.aau.dk, fbl@et.aau.dk, xwa@et.aau.dk.

weak grid, and its active damping strategies have been well investigated recently. A virtual impedance across the grid-side inductance, which can be represented by a series RL branch in parallel with a negative inductance, is added through the grid current feedback control [19]. Refs. [20]-[21] introduced a virtual RC impedance, i.e., the positive resistance to achieve better performance of harmonic resonance damping, and a negative inductance to reduce the grid side inductor for the purpose of better harmonic distortion mitigation. An overview of the virtual impedance based active damping strategy for the grid-connected voltage source and current source converters are summarized in [22], and several alternative methods for implementing the virtual impedance are proposed. The current controller parameters are optimally designed to improve its stability under weak network [23]-[24]. Moreover, the digital control delay is also investigated and mitigated in [25]-[26] in order to improve the converter performance.

Besides the above mentioned series and parallel compensated weak networks, the series π sections weak network is also a possible network configuration [28]-[29]. This kind of weak network consists of series connection of resistances and inductances between both ends of the transmission line, and shunt capacitances are connected between each end and the ground. Unlike the series and parallel compensated weak networks which only have one single magnitude peak, the series π sections have more than one magnitude peak (the same amount of the π sections), resulting in more than one magnitude intersection points between the DFIG system and the weak network, then multiple resonances may occur consequently.

The open-loop transfer function, which is to evaluate and analyze a series of high-frequency resonant peaks in the voltage source inverter due to the high-order LC configuration, is deduced in [28]-[29], then a cascaded notch filters are adopted to suppress the resonant peaks, thus the resonance can be mitigated as a result. Compared with [28]-[29], the main differences in this paper are, 1) different control subjects are discussed, in this paper the authors discuss the DFIG system, while the VSI is discussed in [28]-[29]; 2) different resonance analysis methods are adopted, in this paper the impedance modeling based analysis method is used, while the open-loop transfer function which shows a series of high frequency resonant peaks is used in [28]-[29]; 3) different implementations of active damping, in this paper the virtual impedance inserted in the DFIG stator branch is implemented, while the cascaded notch filter is adopted in [28]-[29]; 4) different operation principles, in this paper the authors intend to reduce the phase difference between the DFIG and the weak network below 180°, while [28]-[29] intend to eliminate the resonant peaks by the cascaded notch filter.

Then, it is clear that the active damping strategies for the HFR in the DFIG system as well as the grid connected converter can be employed to mitigate the MHFR in the DFIG system. The virtual impedance can be introduced to appropriately reshape the impedance of DFIG system, and the detailed explanations on this virtual impedance will be given in following discussion.

It needs to be explained that, 1) the proposed MHFR active damping strategy can be used to mitigate the single HFR since it can be seen as a special case of MHFR; 2) the active damping strategy for the single HFR has been investigated in [18], where the single HFR within a wide frequency range can be mitigated. However this frequency range is smaller than the one for MHFR discussed in this paper, i.e., 1100 Hz to 1600 Hz for single HFR in [18], while 500 Hz to 2500 Hz for MHFR in this paper; 3) Moreover, the virtual impedance for MHFR in this paper is more complicated than the one for single HFR in [18]. In this paper the virtual impedance includes the virtual resistance R_v, phase leading compensation unit with the s^2 and the reciprocal of two-order bandpass filter with the bandpass frequency ω_{bp} and bandwidth parameter ω_c. While for the active damping of single HFR in [18], the virtual impedance contains the virtual resistance R_v, and high-pass filter cutoff frequency f_{cut}. Therefore, it can be concluded that compared with the active damping strategy for single HFR in [18], the active damping for MHFR in this paper has a much wider effective damping frequency range at the cost of more complicated virtual impedance structure.

This paper is organized as follows: the impedance modeling of the DFIG and the Rotor Side Converter (RSC), together with the impedance modeling of the Grid Side Converter (GSC) and the LCL filter, is first established in Section II. The MHFR between the DFIG system and the series π sections weak network is analyzed in Section III, then the proposed active damping strategy in the DFIG stator branch with the introduction of the phase leading compensation unit and the virtual positive resistance are illustrated in details. The simulation setup is built up to validate the MHFR analysis as well as the proposed active damping strategy in Section IV. Finally, the conclusions are given in Section V.

II. Impedance Modeling of DFIG System and Series II Sections Weak Network

Before analyzing the MHFR, the impedance modeling of the DFIG system and the series π section network need to be established first. It should be pointed out that a single DFIG system is discussed in this paper. In a wind farm containing several DFIGs working in parallel, an aggregated modeling of the DFIG system is normally adopted [12]-[15]. For instance, concerning SSR in DFIG, the aggregated DFIG system with 50 single turbines is investigated in [12]-[15]. The difference between a single DFIG and an aggregated DFIG system in [12] is the proportional smaller parameters of the DFIG system. Thus, the proposed MHFR analysis method and the active damping strategy in this paper are still effective in respect to the aggregated DFIG system by adjusting the parameters from a single DFIG to an aggregated DFIG.

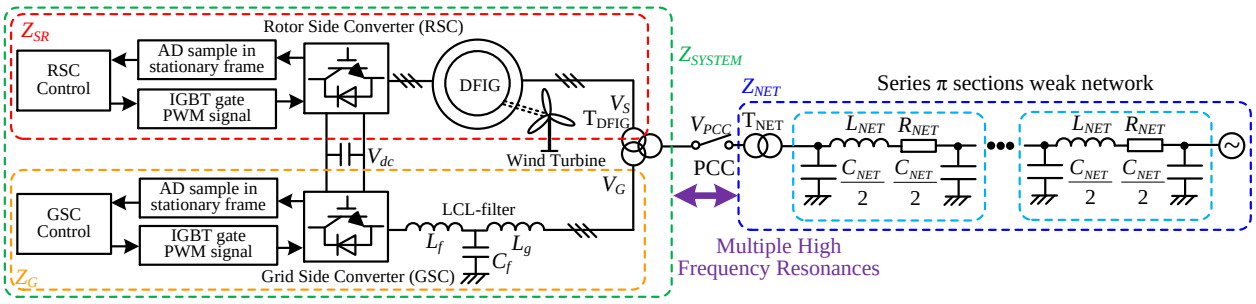

Fig. 1. Diagram of the DFIG system and the series π sections weak network

A. General description of the investigated DFIG system

Fig. 1 shows a diagram of the DFIG system connected to a series π sections weak grid. The RSC controls the rotor voltage to deliver the DFIG stator output active and reactive power, the GSC provides a stable dc-link voltage, and the LCL filter is adopted due to its better switching harmonics filtering performance. A three-terminal step-up transformer T_{DFIG} is connected between the DFIG stator winding, the LCL output terminal and the Point of Common Coupling (PCC) for the purpose of increasing the voltage level of the DFIG system, i.e., GSC output voltage V_G = 480 V, DFIG stator voltage V_S = 690 V, PCC voltage V_{PCC} = 1 kV in this paper. The parameters of this transformer can be found in Table I.

The series π section network contains several single π sections, and the single π section consists of network inductances L_{NET} and network resistances R_{NET} in series connection between both ends of each single section; the network shunt capacitance C_{NET} is connected between each end and the ground. It should be noted that for the sake of simplicity, only two series π sections are shown in Fig. 1 in this paper. The two-terminal transformer T_{NET} is connected between the PCC and the high voltage transmission cable, i.e., PCC voltage V_{PCC} = 1 kV and high voltage V_{HV} = 25 kV in this paper. The parameters of this transformer can be found in Table I.

Note that the transformer T_{DFIG} is connected between the DFIG stator winding and the LCL filter, therefore the leakage inductor of the transformer can be regarded as part of the stator winding inductor and the inductor L_g. By conducting this approximation, the impedance of the DFIG system remains accurate, and the following analysis complexity can be simplified.

B. DFIG system impedance

The grid part of the DFIG system contains the GSC and the LCL filter, thus based on [19], the impedance modeling can be presented as shown in Fig. 2, where $G_c(s\text{-}j\omega_0)$ is the PI controller including the proportional part K_{pgsc} and the integral part $K_{igsc}/(s\text{-}j\omega_0)$. The parameters are available in Table I. $G_d(s\text{-}j\omega_0)$ is the digital control delay of 1.5 sampling periods caused by the voltage/current sampling and the PWM update [19]. ω_0 is the grid network fundamental component angular speed of 100π rad/s, which indicates the reference frame rotation from the stationary frame (where the impedance modeling is built) to the synchronous frame (where the PI closed-loop current control is implemented) as shown in Fig. 1.

Normally, the GSC control has an outer control loop of the dc-link voltage, however due to the slow dynamic response, the dc-link voltage closed-loop control in the GSC is neglected in this paper. The grid synchronization is also neglected in the RSC and GSC control due to similar reasons of slow dynamic responses.

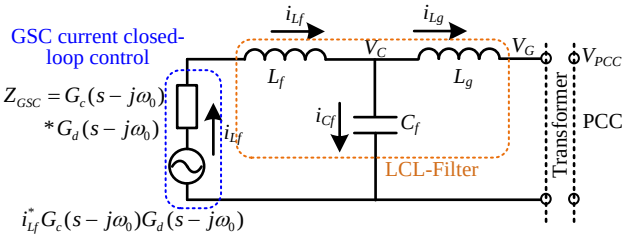

Fig. 2. Impedance modeling of the Grid Side Converter and LCL filter

Thus, as shown in Fig. 2, the impedance of GSC current closed-loop control is modeled as one voltage source $i_{Lf}^* G_c(s\text{-}j\omega_0)G_d(s\text{-}j\omega_0)$ and one impedance $Z_{GSC} = G_c(s\text{-}j\omega_0)G_d(s\text{-}j\omega_0)$ in series.

Then, the impedance of the DFIG grid side, including the GSC, the LCL filter and the transformer, can be obtained as,

$$Z_G = K_1^2 \frac{Z_{Cf}\left(Z_{Lf}+Z_{GSC}\right)+Z_{Lg}\left(Z_{Lf}+Z_{GSC}\right)+Z_{Cf}Z_{Lg}}{Z_{Cf}+\left(Z_{Lf}+Z_{GSC}\right)} \quad (1)$$

where, $Z_{GSC} = G_c(s\text{-}j\omega_0)G_d(s\text{-}j\omega_0)$, $Z_{Cf} = 1/sC_f$, $Z_{Lf} = sL_f$, $Z_{Lg} = sL_g$. C_f is the LCL filter capacitance, L_f is the converter side inductance, L_g is the LCL grid side inductance. K_1 is the voltage ratio between V_G and V_{PCC} as defined $K_1 = V_{PCC}/V_G$.

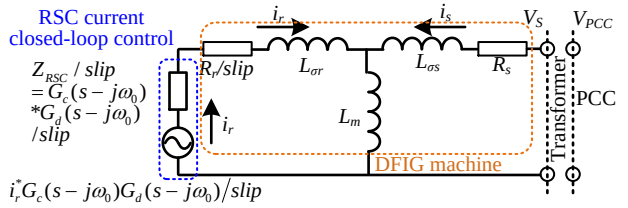

Fig. 3. Impedance modeling of the Rotor Side Converter and DFIG generator

On the other hand, based on [12], the impedance modeling of the RSC and DFIG generator can be obtained in Fig. 3, and it can be obtained as,

$$Z_{SR} = K_2^2 \frac{Z_{Lm}H + (R_s + Z_{L\sigma s})H + Z_{Lm}(R_s + Z_{L\sigma s})}{Z_{Lm} + H} \quad (2)$$

where $H = (R_r + Z_{RSC})/slip + Z_{L\sigma r}$; $Z_{RSC} = G_c(s\text{-}j\omega_0)G_d(s\text{-}j\omega_0)$; $Z_{Lm} = sL_m$; $Z_{L\sigma r} = sL_{\sigma r}$; $Z_{L\sigma s} = sL_{\sigma s}$. R_r is the rotor resistance, L_m is the mutual inductance, $L_{\sigma r}$ is the rotor leakage inductance, $L_{\sigma s}$ is the stator leakage inductance. K_2 is the voltage ratio between V_S and V_{PCC} as defined $K_2 = V_{PCC}/V_S$.

Since the rotor current control and output voltage are both generated in the rotor stationary reference frame, they need to be rotated back to the stationary frame by the slip angular speed as [9]-[12],

$$slip = (s - j\omega_r)/s \quad (3)$$

where, ω_r is the rotor speed.

The impedance of the RSC and DFIG generator Z_{SR} and the impedance of the GSC and LCL filter Z_G are connected in parallel, thus the DFIG system impedance Z_{SYSTEM} can be presented based on (1) and (2) as,

$$Z_{SYSTEM} = \frac{Z_G Z_{SR}}{Z_G + Z_{SR}} \quad (4)$$

A Bode diagram of the RSC and DFIG generator impedance Z_{SR}, the GSC and LCL filter impedance Z_G and the DFIG system impedance Z_{SYSTEM} are plotted in Fig. 4, with the parameters given in Table I. As it can be observed from Fig. 4, the DFIG system impedance Z_{SYSTEM} has a phase response larger than 90° at the frequency above 900 Hz, where the MHFR is most likely to happen and the detailed explanation will be provided in following.

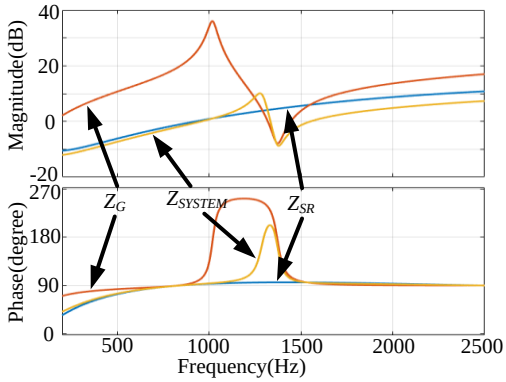

Fig. 4. Bode diagram of the Rotor Side Converter and DFIG generator impedance Z_{SR}, the Grid Side Converter and LCL filter impedance Z_G and the DFIG system impedance Z_{SYSTEM}, the parameters are listed in Table I.

TABLE I. PARAMETERS OF DFIG SYSTEM AND WEAK NETWORK

DFIG generator			
Rated Power	2 MW	T_d	300 μs
R_s	0.0015 Ω	R_r	0.0016 Ω
$L_{\sigma s}$	0.04 mH	$L_{\sigma r}$	0.06 mH
L_m	3 mH	Pole Pairs	3
f_s	5 kHz	f_{sw}	2.5 kHz
LCL filter			
L_g	125 μH	L_f	125 μH
C_f	220 μF		
Current Controller Parameters			
K_{prsc}	0.1	K_{irsc}	2
K_{pgsc}	0.1	K_{igsc}	2
Three-terminal step-up transformer in DFIG system			
V_G	480 V	V_S	690 V
V_{PCC}	1 kV		
$K_1 = V_{PCC}/$	2.08	$K_2 = V_{PCC}/$	1.45
Series π sections weak network			
L_{NET}	36 mH	R_{NET}	2.06 Ω
C_{NET}	1.024 μF		
Two-terminal step-up transformer in weak network			
V_{PCC}	1 kV	V_{HV}	25 kV
$K_3 = V_{HV}/$	25		

C. Series π sections weak network impedance

According to Fig. 1, the impedance of the series π sections weak network Z_{NET} can be presented as,

$$Z_{NET1} = \frac{1}{K_3^2} \frac{(sL_{NET} + R_{NET})/sC_{NET}}{sL_{NET} + R_{NET} + 1/sC_{NET}} \quad (5a)$$

$$Z_{NET2} = \frac{1}{K_3^2} \frac{(sL_{NET} + R_{NET} + Z_{NET1}) * 2/sC_{NET}}{sL_{NET} + R_{NET} + Z_{NET1} + 2/sC_{NET}} \quad (5b)$$

$$Z_{NET3} = \frac{1}{K_3^2} \frac{(sL_{NET} + R_{NET} + Z_{NET2}) * 2/sC_{NET}}{sL_{NET} + R_{NET} + Z_{NET2} + 2/sC_{NET}} \quad (5c)$$

where, R_{NET} and L_{NET} are the network series resistor and inductor, C_{NET} is the network shunt capacitor. Z_{NET1}, Z_{NET2} and Z_{NET3} are the network impedance of only one single π section, two and three π sections respectively. Note that the single π section Z_{NET1} is the same as the parallel compensated weak network discussed in [16]-[17]. K_3 is the voltage ratio between V_{PCC} and high voltage V_{HV} of the transmission cable defined as $K_3 = V_{HV}/V_{PCC}$.

Fig. 5 shows the Bode diagram of a two series π sections weak network impedance Z_{NET2} with C_{NET} = 1.024 or 0.512 μF, R_{NET} = 2.06 Ω, L_{NET} = 36 mH respectively. It needs to be pointed out that the above weak network parameters are calculated based on a long-distance transmission cable, its resistance is 41.2 mΩ / km, inductance is 0.72 mH / km, shunt capacitance is 0.02048 μF / km, the length of per π section is 50 km. These weak network parameters are close to the default values used in Three-Phase PI Section Line Modules in MATLAB Simulink [30], so they can be considered reasonable for the following analysis and simulation validation.

It should be noted that for the sake of simplicity, only Z_{NET2} is taken as an example, while the Z_{NET1} and Z_{NET3} can be similarly described. As it can be seen from Fig. 5, due to the two π sections in series connection, the weak network has two magnitude peaks. Apart from the magnitude peak range, the phase response of the weak network is either 90° or -90°. Since the phase response of the DFIG system is always 90° at frequency above 900 Hz as shown in Fig. 4, the resonances will occur when the magnitude intersection points are located in the range where the phase response of the weak network is -90°.

By comparing the impedance shape of the series π sections weak network with two different network shunt capacitances C_{NET} = 1.024 or 0.512 μF in Fig. 5, it can be

found that the magnitude peak shifts towards higher frequency range as the C_{NET} becomes smaller. This character results in the higher MHFR frequency when C_{NET} becomes smaller.

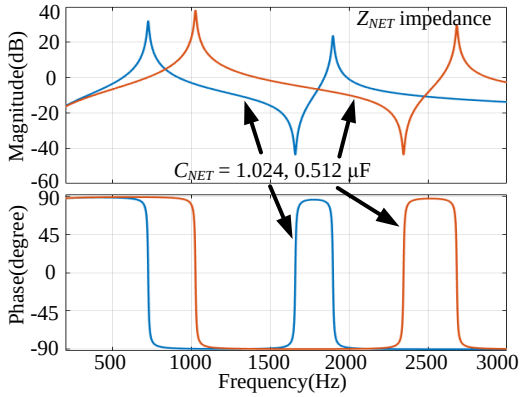

Fig. 5. Bode diagram of the series π sections weak network impedance with C_{NET} = 1.024 or 0.512 μF, R_{NET} = 2.06 Ω, L_{NET} = 36 mH

III. MHFR AND ACTIVE DAMPING STRATEGY

Based on the impedance modeling of the DFIG system and the series π sections weak network, the MHFR can be analyzed in this section. Moreover, the active damping strategy based on the virtual impedance also needs to be introduced to effectively mitigate the MHFR.

A. *MHFR Analysis*

As reported in [16]-[18], a phase difference of 180° between the DFIG system and the weak network at the magnitude intersection point will result in the resonance. The DFIG system behaves inductive with the phase response of 90° at frequencies above 900 Hz as shown in Fig. 4, thus the phase response of -90° in the weak network is prerequisite for the resonance.

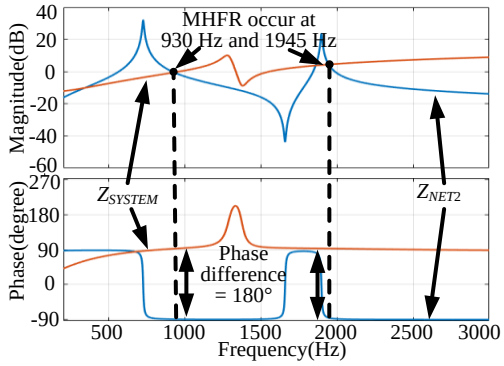

Fig. 6. Bode diagram of the DFIG system in Table I and the series π sections weak network impedance with C_{NET} = 1.024 μF, R_{NET} = 2.06 Ω, L_{NET} = 36 mH.

Fig. 6 shows the Bode diagram of the DFIG system with its parameters given in Table I and the series π sections weak network impedance with C_{NET} = 1.024 μF, R_{NET} = 2.06 Ω, L_{NET} = 36 mH.

As it is shown in Fig. 6, there are two magnitude intersection points between the DFIG system and the series π sections weak network at 930 Hz and 1945 Hz respectively, and the phase difference is 180° at both these frequencies. Consequently, the MHFR at 930 Hz and 1945 Hz will occur.

It should be noted that besides the above resonance frequencies, there exists additional two magnitude intersection points at 340 Hz and 1860 Hz. However no resonances at these frequencies will be produced since the phase difference is smaller than 180°, instead the sufficient phase margin will ensure a stable DFIG system operation at these frequencies. The above analysis will be validated by the simulation results in the following parts.

B. *Active damping strategy*

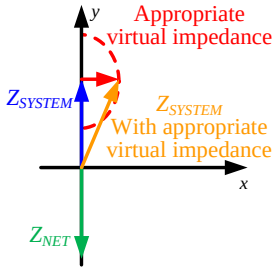

Fig. 7. Vector diagram of the expected impedance reshaping

Fig. 7 gives out the vector diagram of the expected impedance reshaping of the DFIG system. As it can be observed, if the virtual impedance is appropriately kept within the phase response of -90° to 90° (right half plane), then the phase difference between the reshaped DFIG system and the weak network can be reduced smaller than 180°, and the MHFR can effectively be mitigated. Note that in the following discussion, the expected phase response of the virtual impedance is set to 0°, i.e., virtual positive resistance as shown in Fig. 7 and then consequently almost the largest phase margin can be obtained.

Before introducing the virtual impedance, it should be pointed out that, the digital control delay exists all the time in the DFIG system as presented in (6). As a consequence, the phase delay will inevitably be introduced to the virtual impedance.

$$G_d(s) = e^{-sT_d} \tag{6}$$

where, the control delay is 1.5 sampling periods [19], T_d = 300 μs, T_s = 200 μs is the sampling period according to Table I.

The digital control delay causes a phase delay $\Delta\theta$ in the potential MHFR range according to (7), and the vector diagram can be plotted as shown in Fig. 8.

$$\Delta\theta = -2\pi f T_d \tag{7}$$

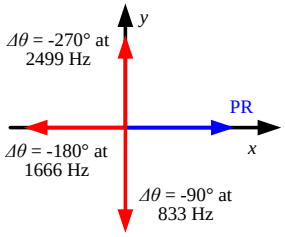

Fig. 8. Vector diagram of phase delay caused by the digital control delay T_d = 300 μs

According to (7) and Fig. 8, it can be found out that the phase delay is only determined by the digital control delay

T_d, and the delay is linear to the frequency.

In order to introduce the virtual positive resistance with the phase response of 0°, the phase delay caused by the digital control delay needs to be appropriately compensated by the phase leading compensation unit.

In order to achieve the phase response increasing as the frequency increases, the reciprocal of the bandpass filter is adopted here due to its phase = -90° below ω_{bp}, 0° at ω_{bp}, and 90° above ω_{bp}, which finally can be presented as,

$$\frac{1}{G_{bp}(s)} = \frac{s^2 + 2\omega_c s + \omega_{bp}^2}{2\omega_c s} \tag{8}$$

where, ω_{bp} is the bandpass frequency, ω_c is the bandwidth.

Besides (8), the additional phase leading of 180° is still required, thus the phase leading unit $G_{lead}(s)$ can be deduced by combining (8) and s^2 as,

$$G_{lead}(s) = \frac{s^2}{G_{bp}(s)} = \frac{s^2\left(s^2 + 2\omega_c s + \omega_{bp}^2\right)}{2\omega_c s} \tag{9}$$

Fig. 9 shows the Bode diagram of the proposed phase leading compensation unit $G_{lead}(s)$, with ω_c = 2000 rad/s, ω_{bp} = 2π*1600 rad/s. It can be observed from Fig. 9 that within the potential MHFR range of 800 Hz to 2400 Hz, the phase response of the proposed phase leading compensation unit is close to linear. For instance, the phase = 105° at 800 Hz, and 245° at 2400 Hz. These two phase responses indicate that the phase delay in Fig. 8 can be appropriately compensated, and the phase response after compensation will be within ±20°, which is beneficial to the DFIG system impedance reshaping as shown in Fig. 7.

Besides, the magnitude of the phase leading compensation is also within 160 dB to 170 dB at the interested frequency range, thus ensuring almost the same impedance reshaping within these frequency ranges.

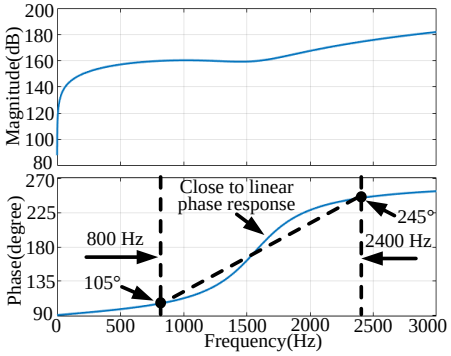

Fig. 9. Bode diagram of the proposed phase leading compensation unit, with ω_c = 2000 rad/s, ω_{bp} = 2π*1600 rad/s.

Thus, based on (9) and (6), the proposed virtual impedance $Z_v(s)$ can be presented as,

$$Z_v(s) = R_v G_{lead}(s) G_d(s) = R_v \frac{s^2\left(s^2 + 2\omega_c s + \omega_{bp}^2\right)}{2\omega_c s} e^{-sT_d} \tag{10}$$

where, R_v is the virtual positive resistance, digital control delay T_d is also included in this equation in order to better show the phase response of the virtual impedance.

According to Fig. 9, the proposed phase leading compensation unit has large magnitude response due to the adoption of s^2. Here, the virtual resistance R_v can be regarded as such a constant coefficient, and designed as a very small constant R_v = 4e-9 Ω in order to adjust the magnitude of the virtual impedance close to the magnitude of the DFIG system, then the appropriate impedance reshaping can be achieved.

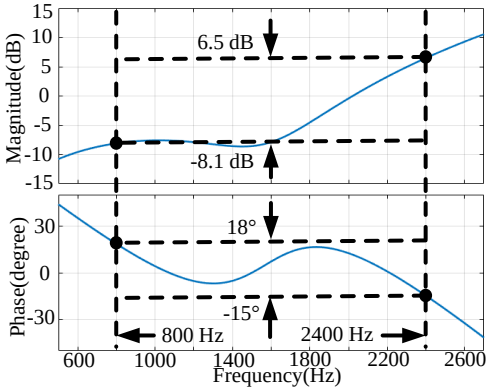

Fig. 10. Bode diagram of the proposed virtual impedance Z_v, with ω_c = 2000 rad/s, ω_{bp} = 2π*1600 rad/s, R_v = 4e-9 Ω, T_d = 300 μs

Fig. 10 shows the Bode diagram of the proposed virtual impedance Z_v, with ω_c = 2000 rad/s, ω_{bp} = 2π*1600 rad/s, R_v = 4e-9 Ω, T_d = 300 μs. As it is shown in Fig. 10, the phase response of the proposed virtual impedance is between -15° and 18° within the frequency range between 800 Hz and 2400 Hz. This phase response is close to 0° as expected in Fig. 7, indicating that the phase leading compensation unit is capable of compensating the phase delay caused by the digital control delay. Moreover, the magnitude response is kept between -8.1 dB to 6.5 dB, which is close to the DFIG system magnitude response. As a result the proposed virtual impedance can have distinct influence on the DFIG system impedance reshaping.

As it can be observed from (10) and Fig. 10, due to the "s" in the numerator, the magnitude response of the virtual impedance decreases as the frequency decreases. This means that the proposed virtual impedance has negligible influence on the rotor current fundamental component closed-loop control in the RSC and the original dynamic performance of the rotor current controller can be maintained.

Then, it can be concluded that, due to the appropriate magnitude and phase response of the proposed virtual impedance shown in Fig. 10, the appropriate reshaping of the DFIG system can be achieved, and a sufficient phase margin can be produced, which will be proved in the following.

C. Parameter design of the virtual impedance

According to (10), the parameters of R_v, ω_{bp} and ω_c need to be designed for the virtual impedance.

1) Design of ω_{bp}

As it is analyzed in Fig. 6, under the specific weak network discussed in this paper, the potential resonance frequency range is between 500 Hz and 2500 Hz and the bandpass frequency ω_{bp} should be chosen around the central frequency of ω_{bp} = 2π*1600 rad/s.

2) Design of ω_c

The phase response of the phase leading compensation

unit in (9) is used to compensate the phase delay caused by the digital control delay as shown in Fig. 8.

Thus, as shown in Fig. 8 and Fig. 9, the phase response of the phase leading compensation unit in (9) is expected to be linearly increasing as the frequency increases, thus the ω_c can be designed on the basis of the expected linear phase response.

By substituting $s = j\omega_0$ into (9) yields the following equation,

$$G_{lead}(j\omega_0) = \frac{j\omega_0\left(\omega_{bp}^2 - \omega_0^2 + j2\omega_c\omega_0\right)}{2\omega_c} = \frac{-2\omega_c\omega_0^2 + j\omega_0\left(\omega_{bp}^2 - \omega_0^2\right)}{2\omega_c} \quad (11)$$

Then, the phase response of (11) can be presented as,

$$\angle G_{lead}(j\omega_0) = \tan^{-1}\left(\frac{\omega_{bp}^2 - \omega_0^2}{-2\omega_c\omega_0}\right) = \theta_{\exp} \quad (12)$$

where, θ_{exp} is the expected phase response at the frequency of ω_0.

Taking the frequency ω_0 = 2π*800 Hz and the corresponding phase response θ_{exp} = 105° (which is determined by the digital control delay in Fig. 8) as an example, the ω_c can be calculated according to (12) as ω_c = 2020 rad/s; similarly, when ω_0 = 2π*2400 Hz and θ_{exp} = 245°, the ω_c can be calculated according to (12) as ω_c = 1953 rad/s. Thus, in this paper, the ω_c is designed as ω_c = 2000 rad/s as shown in Fig. 9.

3) Design of R_v

As shown in Fig. 9, the proposed phase leading compensation unit has a large magnitude response due to the adoption of s^2. This large magnitude response can be appropriately adjusted by a constant coefficient. Here, the virtual resistance R_v can be regarded as such a constant coefficient, and R_v is designed as a small constant R_v = 4e-9 Ω in order to adjust the magnitude of the virtual impedance close to the magnitude of the DFIG system. Then the virtual impedance can have distinctive influence on the DFIG system, and an appropriate impedance reshaping can be achieved. Note that the designing of R_v should not be too small (otherwise no obvious influence will be produced in the rotor part impedance), and not too large (otherwise the grid part impedance will play dominant role in determining the overall DFIG system impedance, and no enough phase margin can be produced). The detailed discussion on the R_v concerning the phase margin and the mitigation of MHFR will be conducted in Section III. E.

D. Implementation of virtual impedance in the stator branch

Once the virtual impedance is obtained as shown in (10), it is also important to implement this virtual impedance to the DFIG system.

According to Fig. 3, the rotor branch is in parallel connection with the mutual inductor branch, therefore the proposed virtual impedance will be subject to the mutual inductor value and pose less influence on the DFIG impedance reshaping if it is implemented in the rotor side. In contrast, the virtual impedance can have more significant influence on the DFIG impedance reshaping if it is proposed in the stator side as shown in Fig. 11.

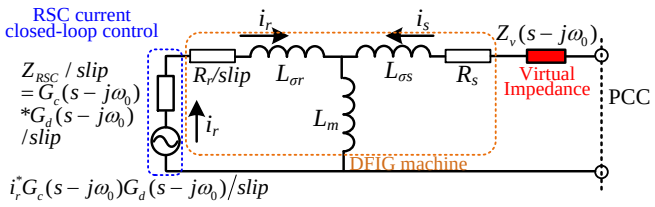

Fig. 11. Impedance modeling of RSC and DFIG generator with the introduction of virtual impedance in DFIG stator current feedforward control

By introducing the virtual impedance Z_v, the DFIG and RSC impedance Z_{SRv}, the total DFIG system impedance $Z_{SYSTEMv}$ can be presented as,

$$Z_{SRv} = \frac{Z_{Lm}H + \left(R_s + Z_{L\sigma s} + Z_v\right)H + Z_{Lm}\left(R_s + Z_{L\sigma s} + Z_v\right)}{Z_{Lm} + H} \quad (13a)$$

$$Z_{SYSTEMv} = \frac{Z_G Z_{SRv}}{Z_G + Z_{SRv}} \quad (13b)$$

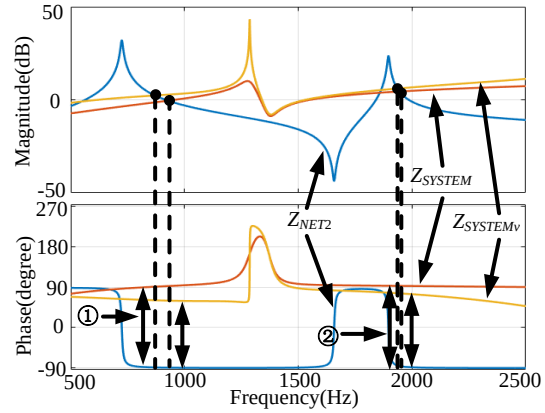

① Phase difference = 180° at 930 Hz → 150° at 870 Hz
② Phase difference = 180° at 1945 Hz → 166° at 1934 Hz

(a)

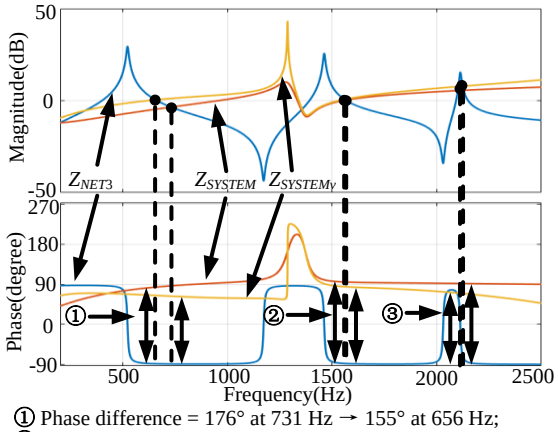

① Phase difference = 176° at 731 Hz → 155° at 656 Hz;
② Phase difference = 185° at 1564 Hz → 174° at 1558 Hz;
③ Phase difference = 166° at 2128 Hz → 142° at 2124 Hz;

(b)

Fig. 12. Bode diagram of the DFIG system impedance and the series π sections weak network Z_{NET} (a) two sections Z_{NET2}; (b) three sections Z_{NET3}, with C_{NET} = 1.024 μF, R_{NET} = 2.06 Ω, L_{NET} = 36 mH in (5). Virtual impedance in (10) with ω_c = 2000 rad/s, ω_{bp} = 2π*1600 rad/s, R_v = 4e-9 Ω, T_d = 300 μs

Fig. 12 shows the Bode diagram of the DFIG system impedance and the series π sections weak network Z_{NET} (a) two sections Z_{NET2}; (b) three sections Z_{NET3}, with C_{NET} = 1.024 μF, R_{NET} = 2.06 Ω, L_{NET} = 36 mH in (5). The virtual impedance in (10) is introduced with ω_c = 2000 rad/s, ω_{bp} = 2π*1600 rad/s, R_v = 4e-9 Ω, T_d = 300 μs.

As it can be seen from Fig. 12(a), before the virtual impedance is implemented, the phase differences between the DFIG system and the two series π sections weak network Z_{NET2} at 930 Hz and 1945 Hz are 180°, which causes two resonances.

Once the virtual impedance is introduced, due to the phase response of the virtual impedance around 10° at 930 Hz and 1945 Hz in Fig. 10, the phase difference can be reduced to 150° at 870 Hz and 166° at 1934 Hz. Therefore, the original two MHFRs can be mitigated as a result.

Furthermore, the case of three π sections weak network is also shown in Fig. 12(b). It can be observed that the lower magnitude intersection at 731 Hz has a phase difference of 176°, thus no resonance occurs at this frequency; the proposed virtual impedance is capable of reducing the phase difference to 155° at 656 Hz.

While the middle resonance occurs at 1564 Hz due to the phase difference of 185°, by introducing the virtual impedance, the phase difference can be successfully reduced to 174° at 1558 Hz, and the middle resonances can be well mitigated as a result. Note that the phase margin can be further increased by appropriately increasing the virtual positive resistance R_v.

The magnitude intersection at 2128 Hz is similar to the first one, and the phase difference at 2128 Hz is 166°, resulting in no resonance, and the phase difference can still be reduced to 142° at 2124 Hz, which helps to validate the effectiveness of the proposed virtual impedance.

Based on the above analysis, it can be concluded that, there are two advantages of the proposed active damping control strategy:

1) No unit for accurate resonance frequency detection is required, instead it is only needed to estimate the approximate MHFR frequency, like between 500 Hz and 2500 Hz in this paper and thereby the control complexity can be reduced.

Moreover, if the grid impedance changes due to the source and load switching, and as long as the potential MHFR frequency remains within the range of 500 Hz to 2500 Hz, the proposed active damping strategy is still able to mitigate the HFR, meaning the predesigned parameters are still effective.

However, if a too large grid impedance change is seen and causes a large resonance frequency change, then the virtual impedance parameters may need to be re-designed. This can be seen as a limitation of the proposed active damping strategy;

2) The MHFR within a certain frequency range, rather than single resonance frequency, can be effectively mitigated by introducing the virtual impedance. This virtual impedance can be considered as a virtual positive resistance with phase response close to 0° and thus the phase difference between the DFIG system and the weak network can be reduced to smaller than 180°.

E. Discussion on the virtual resistance R_v

According to (10), the virtual resistance R_v is very important to the amplitude of the virtual impedance. Thus, it is meaningful to discuss the influence of R_v on the phase margin and the mitigation of MHFR when the active damping strategy is enabled.

The authors would like to explain this problem from the following three aspects, with the resonance in 1558 Hz shown in Fig. 12 as an example,

1) On one hand, as it is shown in Fig. 13, the increasing of the R_v from 4e-9 Ω (in red) to 8e-9 Ω (in yellow) and to 16e-9 Ω (in purple) helps to reduce the phase difference between the DFIG system and the weak network from 174° at 1558 Hz, to 168° at 1548 Hz, and to 168° at 1534 Hz. Thus, it can be seen that the increasing of R_v helps to increase the phase margin to certain extent and better mitigation of the MHFR can be achieved.

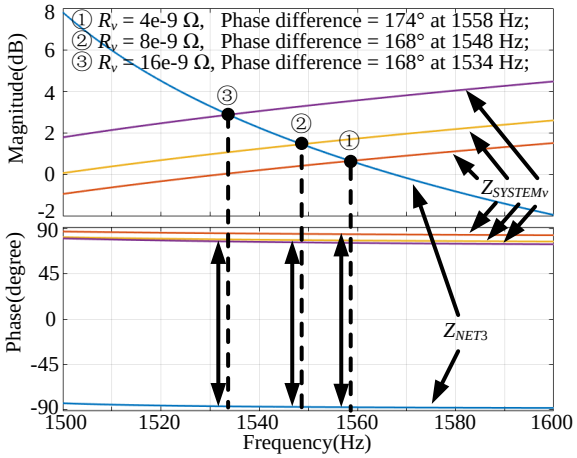

Fig. 13. Bode diagram of the DFIG system impedance with virtual impedance in (10) with ω_c = 2000 rad/s, ω_{bp} = 2π*1600 rad/s, T_d = 300 μs, R_v = 4e-9 Ω, 8e-9 Ω, 16e-9 Ω.

2) On the other hand, the virtual impedance is inserted into the DFIG stator branch as shown in Fig. 11, and the DFIG rotor part impedance (which contains the virtual impedance) will be connected in parallel with the grid part impedance as shown in Fig. 1.

According to the electric circuit principle, the overall impedance of the DFIG system (including both the rotor part and the grid part) is mainly determined by the one with smaller impedance. Since the rotor part impedance becomes larger due to the insertion of virtual impedance shown in Fig. 14, therefore the overall impedance of the DFIG system is mainly determined by the grid part impedance if too large virtual impedance is inserted into the stator branch.

As a consequence, the virtual impedance in the stator branch has limited influence on the DFIG system impedance reshaping, and thus limited phase margin can be achieved. This point can be further explained from Fig. 13 that when the R_v becomes too large as R_v = 16e-9 Ω, it does not cause further phase response decreasing but remains the same phase margin as the case of R_v = 8e-9 Ω, and the

largest phase margin can be achieved as 168° at 1548 Hz when R_v = 8e-9 Ω.

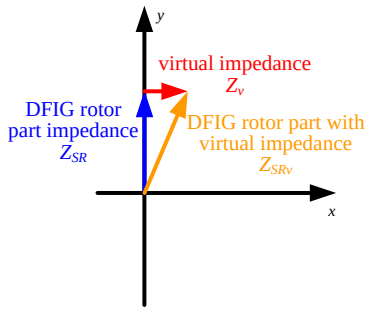

Fig. 14. Vector diagram of the DFIG system impedance and the virtual impedance

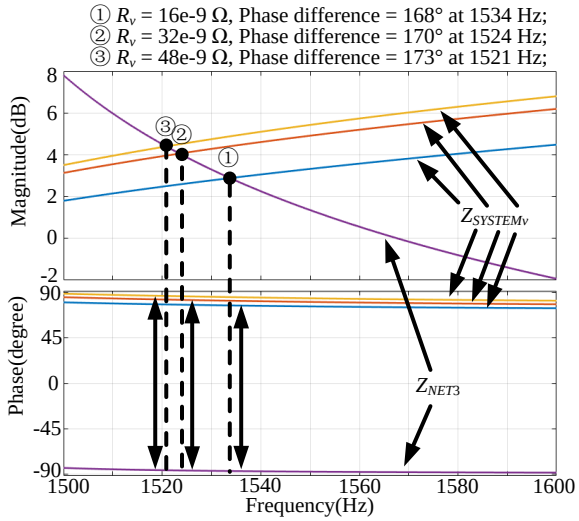

Fig. 15. Bode diagram of the DFIG system impedance with virtual impedance in (10) with ω_c = 2000 rad/s, ω_{bp} = 2π*1600 rad/s, T_d = 300 μs, too large R_v = 16e-9 Ω, 32e-9 Ω, 48e-9 Ω.

Furthermore, when even larger R_v is adopted as R_v = 16e-9 Ω, 32e-9 Ω, 48e-9 Ω, the phase difference unfortunately becomes larger as shown in Fig. 15, i.e., 168° at 1534 Hz when R_v = 16e-9 Ω, 170° at 1524 Hz when R_v = 32e-9 Ω, 173° at 1521 Hz when R_v = 48e-9 Ω. The reason for this performance is that, as the virtual impedance in the stator branch becomes larger, the grid side impedance plays a more and more important role in determining the overall DFIG system impedance. As a result, the phase response of the DFIG system goes closer and closer to 90° and the phase margin becomes smaller.

3) One more thing is that, it is important to ensure that the introduction of the virtual impedance does not cause any influence on the normal operation of the rotor current control. Thus, too large R_v is not preferred since the too large R_v will unfortunately cause certain influence on the rotor current control.

Therefore, based on above discussion, it can be seen that the designing of R_v should not be too small (otherwise no obvious influence will be produced in the DFIG system impedance reshaping), and not too large (otherwise the grid part impedance will play dominant role in determining the overall DFIG system impedance, and no enough phase margin can be produced).

F. Control block diagram

Fig. 16 shows the control block diagram of the DFIG system MHFR active damping strategy through the virtual impedance implemented in the stator current feedforward control. As it can be seen, for the RSC control, an Enhanced Phase Locked Loop (EPLL) [4]-[6] is able to provide the information of the grid voltage fundamental synchronous angular speed ω_1 and angle θ_1, while an encoder gives out the DFIG rotor position θ_r and speed ω_r. The rotor current $\boldsymbol{I}^+_{rdq}$ is first sampled and then controlled according to the reference value $\boldsymbol{I}^{+*}_{rdq}$ by a PI controller to output the harvested wind energy. The stator current $\boldsymbol{I}^+_{sdq}$ is also sampled for the feedforward control with the introduction of the virtual impedance. The output of the rotor current PI closed-loop control $\boldsymbol{V}^+_{rdqPI}$ and the output of virtual impedance resonance damping $\boldsymbol{V}^+_{sdqv}$, are added, together with the decoupling compensation, giving out the rotor control voltage $\boldsymbol{V}^+_{rdq}$, which is then transformed to the rotor stationary frame and delivered as the input to the Space Vector Pulse Width Modulation (SVPWM).

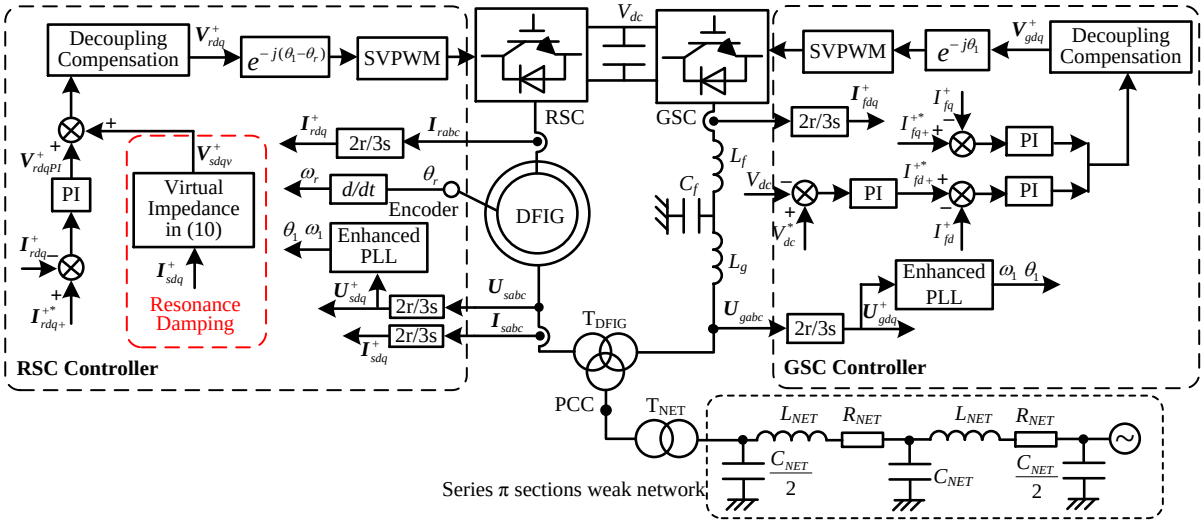

Fig. 16. Control block diagram of the DFIG system MHFR active damping strategy through virtual impedance.

As for the GSC control, the dc-link voltage V_{dc} is well regulated by a PI controller, and its output is delivered as the converter side inductance filter current reference $\boldsymbol{I}_{fdq}^{+*}$, which is used to regulate the actual converter side inductance filter current $\boldsymbol{I}_{fdq}^{+}$ by a PI controller. Similarly, the GSC control voltage $\boldsymbol{V}_{gdq}^{+}$ can be obtained by the PI current controller output and the decoupling compensation unit.

IV. Simulation Validation

In order to validate the proposed MHFR active damping strategy, a simulation model is built up, the control block is shown in Fig. 16, and the DFIG system parameters can be found in Table I. The rotor speed is set to 800 rpm (0.8 p.u.), with synchronous speed of 1000 rpm (1.0 p.u.). The dc-link voltage is 1200 V. The switching frequency f_{sw} for both RSC and GSC is 2.5 kHz, the sampling frequency f_s for both RSC and GSC is 5 kHz.

Fig. 17 shows the simulation results of MHFR in the DFIG system under sub- synchronous speed (800 rpm, 0.8 p.u.) (a) steady state when the active damping strategy is disabled; (b) steady state when the active damping strategy is enabled; (c) transient state at the instance of enabling the active damping strategy; (d) FFT analysis result of the steady state response.

As shown in Fig. 17(a), when the active damping strategy is disabled, the MHFR occurs at 952 Hz and 1977 Hz in the entire DFIG system, including the stator voltage and current, rotor current, grid side current, stator output power and grid side output power. The simulation results match well with the theoretical analysis in Fig. 6 as 930 Hz and 1945 Hz. According to the stator voltage distortion analysis shown in Fig. 17(d), the MHFR consists mainly of 952 Hz (6.9%) and 1977 Hz (45.9%) components. Thus, the simulation result is able to verify the analysis of the impedance interaction based MHFR in the DFIG system connected to the series π sections weak network.

It should be noted that the amplitude of the resonance is determined by the equivalent resistance of both the DFIG system and the weak network at the resonance frequency. This indicates that a smaller value of the equivalent resistance will result in a larger amplitude of the resonance. For instance, when the equivalent resistance at 952 Hz is 10 times larger than the equivalent resistance at 1977 Hz, then a larger amplitude of the resonance at 1977 Hz will occur compared to the resonance at 952 Hz.

In practice, the equivalent resistance at the resonance frequency is subject to several factors, which are involved in the impedance expression, including the parameters of the DFIG machine and the LCL filter, the weak network parameters and the current controller parameters. Therefore, the amplitude of the resonance is not discuss in detail in this paper.

Once the active damping strategy is enabled, the MHFR can be successfully mitigated, with an obvious improvement in the DFIG system variables observed from Fig. 17(b). The stator voltage distortion analysis result is shown in Fig. 17(d), where the previous large resonance components in the stator voltage can be well mitigated as 952 Hz: 0.8%, 1977 Hz: 1.1%, which are sufficiently small to be neglected. Besides, the stator current, rotor current and grid current become much more sinusoidal, the stator output power and grid side output power become much smoother. Thus, the effectiveness of the proposed active damping strategy can be validated.

Fig. 17(c) shows the transient response at the instance of enabling the active damping strategy. It can be observed that, before enabling, the large resonance components exist in the DFIG system; however, once the active damping strategy is enabled, it is able to mitigate the resonance components within 20 ms. Thereby, a good dynamic performance of the proposed active damping strategy can be validated, and makes this strategy applicable in the practical cases.

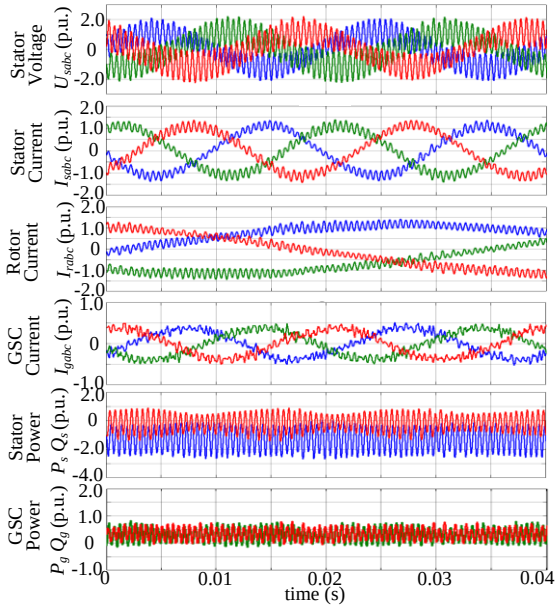

(a)

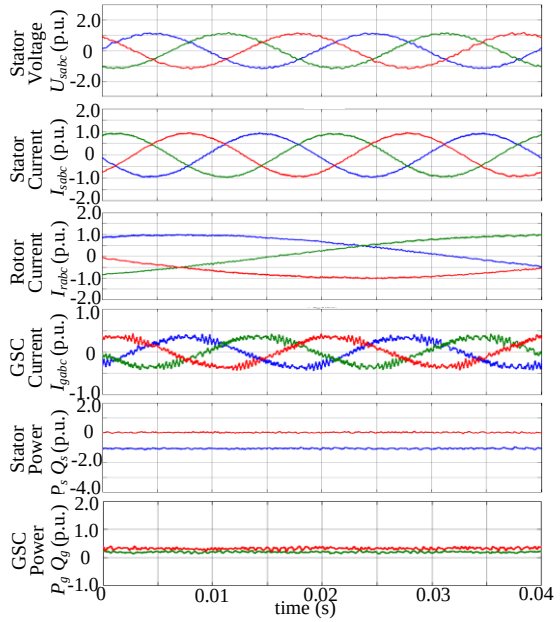

(b)

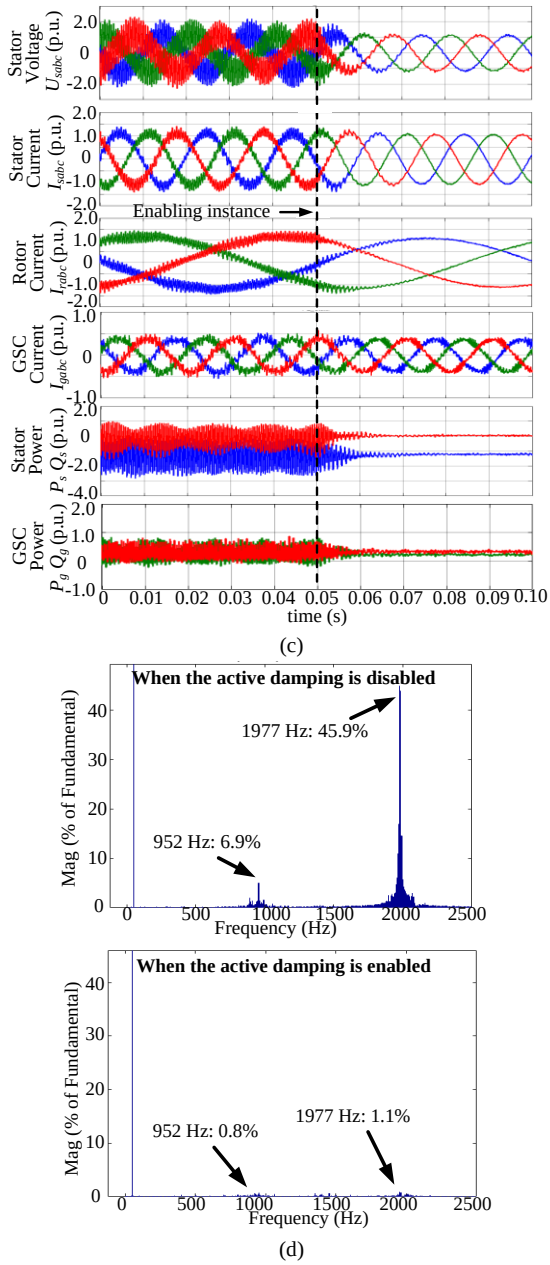

Fig. 17. Simulation results of MHFR in the DFIG system under sub-synchronous speed (800 rpm, 0.8 p.u.), steady state when the active damping strategy is (a) disabled; (b) enabled; (c) transient state at the instance of enabling the active damping strategy; (d) FFT analysis of steady state response.

Based on the simulation results in Fig. 17, the theoretical analysis of MHFR, which is caused by the impedance interaction between the DFIG system and the series π sections weak network, can be verified. Moreover, the proposed active damping strategy with the introduction of the phase leading compensation unit and virtual positive resistance is proved to be able to mitigate the MHFR by reducing the phase difference and producing an appropriate phase margin.

Besides the non-divergent MHFR in the DFIG system shown in Fig. 17, the divergent MHFR is also possible to occur. Hence, it is meaningful to discuss the active damping strategy under the circumstance of divergent MHFR. The following simulations regarding the divergent MHFR are conducted with the same parameters as the case in Fig. 17, but only different parameters of weak network shunt capacitance is half value of the Fig. 17, that is, C_{NET} = 0.512 μF.

Fig. 18 shows the simulation result of divergent MHFR when the active damping strategy is disabled. It can be seen that the DFIG system fails to operate stable, and divergence with extreme large amplitude of stator voltage and current, rotor current and output power can be seen. In practice, such performance will trigger the over-voltage and over-current protection, while the simulation results are shown here in order to show the occurrence of DFIG system divergence. The FFT analysis shows that the divergence mainly contains the resonance components at 2720 Hz of 61.2 p.u. of fundamental component.

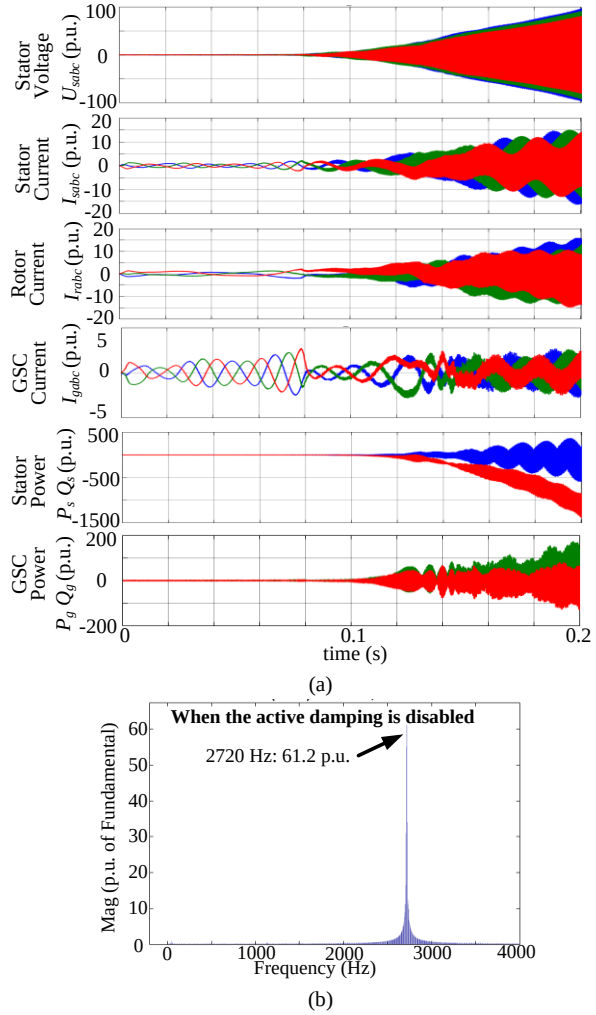

Fig. 18. Simulation results of divergent MHFR in the DFIG system under sub- synchronous speed (800 rpm, 0.8 p.u.), steady state when the active damping strategy is disabled; (a) system performance; (b) FFT analysis of stator voltage.

Fig. 19 shows the simulation result of divergent MHFR when the active damping strategy is enabled at 0.1s. Note that the divergence starts to develop at 0 s, and the divergence is still not so large by the time of 0.1 s and the DFIG system can still be brought back to stability at 0.1 s.

It can be seen that once the active damping strategy is enabled at 0.1 s, the stator voltage with the divergence amplitude around 6 p.u. can be suppressed, and the other

variables including the stator current, rotor current, output power can all be brought back to stable operation. The FFT analysis of stator voltage shows the resonance components of 2800 Hz: 17.6% and 1175 Hz: 1.6%.

Therefore, by comparing the simulation results in Fig. 18 and Fig. 19, it can be concluded that the proposed active damping strategy is able to suppress the divergence MHFR in the DFIG system and bring the system back to stable operation, which is beneficial to the practical performance of the DFIG system.

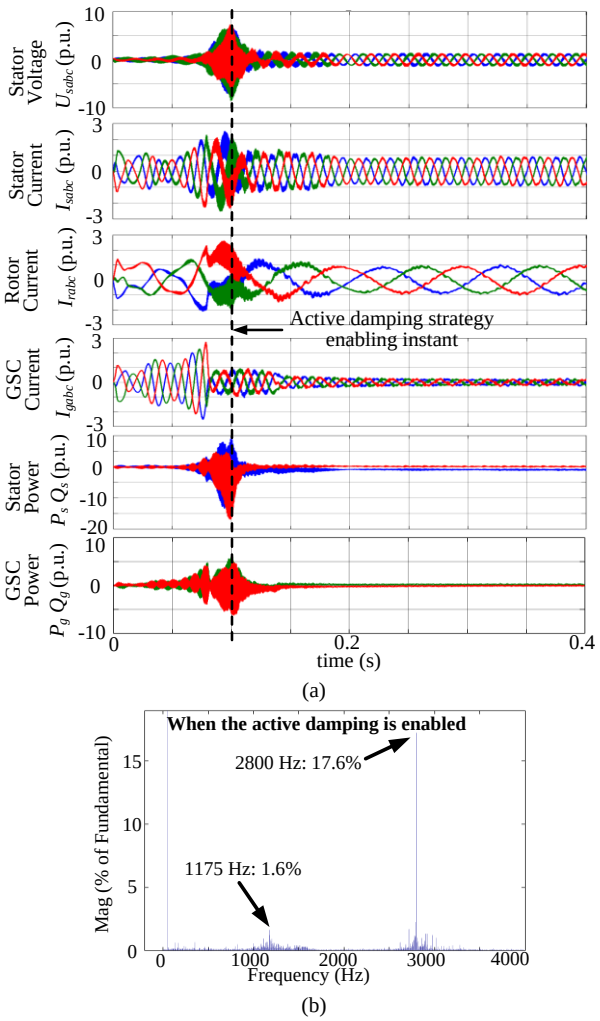

Fig. 19. Simulation results of divergent MHFR in the DFIG system under sub- synchronous speed (800 rpm, 0.8 p.u.), steady state when the active damping strategy is enabled; (a) system performance; (b) FFT analysis of stator voltage.

V. Conclusion

This paper has performed the analysis of the MHFR in the DFIG system under series π sections weak network, and proposed an active damping strategy based on the introduced virtual impedance, which consists of the phase leading compensation unit and the virtual positive resistance. Several conclusions can be drawn as,

1) The MHFR occurs when the DFIG system is connected to the series π sections weak network due to the phase difference of 180° at the multiple magnitude intersection points;

2) The proposed virtual impedance, which consists of a phase leading compensation unit and a virtual positive resistance, can appropriately reshape the DFIG system impedance, and mitigate the resonances by reducing the phase difference and producing appropriate phase margin;

3) The proposed active damping strategy is able to simultaneously mitigate the multiple resonances within a certain wide frequency range, and fast dynamic performance can be ensured.

REFERENCES

[1] F. Blaabjerg, and K. Ma, "Future on Power Electronics for Wind Turbine Systems," *IEEE J. Emer. Sel. Topics Power Electron*., vol. 1, no. 3, pp. 139-152, Sep. 2013.

[2] K. Ma, L. Tutelea, I. Boldea, D. M. Ionel, F. Blaabjerg, "Power Electronic Drives, Controls, and Electric Generators for Large Wind Turbines–An Overview", *Electric Power Components and Systems*, vol. 43, no. 12, pp. 1406-1421, 2015.

[3] V. Yaramasu, B. Wu, P. C. Sen, S. Kouro, and M. Narimani, "High-power wind energy conversion systems: State-of-the-art and emerging technologies," *Proceedings of the IEEE*, vol. 103, no. 5, pp. 740 – 788, 2015.

[4] H. Nian, P. Cheng, and Z. Q. Zhu, "Coordinated Direct Power Control of DFIG System Without Phase-Locked Loop Under Unbalanced Grid Voltage Conditions," *IEEE Trans. Power Electron*., vol. 31, no. 4, pp. 2905 - 2918, Apr. 2016.

[5] Y. Song, H. Nian, "Modularized Control Strategy and Performance Analysis of DFIG System Under Unbalanced and Harmonic Grid Voltage," *IEEE Trans. Power Electron.*, vol. 30, no. 9, pp. 4831 - 4842, Sept. 2015.

[6] H. Nian, Y. Song, "Direct Power Control of Doubly Fed Induction Generator Under Distorted Grid Voltage," *IEEE Trans. Power Electron.*, vol. 29, no. 2, pp. 894-905, Feb. 2014.

[7] R. Zhu, Z. Chen, Y. Tang, F. Deng, and X Wu, "Dual-Loop Control Strategy for DFIG-Based Wind Turbines Under Grid Voltage Disturbances," *IEEE Trans. Power Electron*., vol. 31, no. 3, pp. 2239 - 2253, Mar. 2016.

[8] W. Chen, F. Blaabjerg, N. Zhu, M. Chen, and D. Xu, "Doubly Fed Induction Generator Wind Turbine Systems Subject to Recurring Symmetrical Grid Faults," *IEEE Trans. Power Electron*., vol. 31, no. 2, pp. 1143 - 1160, Feb. 2016.

[9] I. Vieto, and J. Sun, "Damping of Subsynchronous Resonance Involving Type-III Wind Turbines," *in Proc. Control and Modeling for Power Electronics* (COMPEL), pp. 1-8, 2015.

[10] I. Vieto, and J. Sun, "Small-Signal Impedance Modeling of Type-III Wind Turbine," *in Proc. Power & Energy Society General Meeting* (PESG), pp. 1-5, 2015.

[11] I. Vieto, and J. Sun, "Real-time Simulation of Subsynchronous Resonance in Type-III Wind Turbines," *in Proc. Control and Modeling for Power Electronics* (COMPEL), pp. 1-8, 2014

[12] Z. Miao, "Impedance-Model-Based SSR Analysis for Type 3 Wind Generator and Series-Compensated Network," *IEEE Trans. Energy Convers.*, vol. 27, no. 4, pp. 984–991, Dec. 2012.

[13] L. Piyasinghe, Z. Miao, J. Khazaei, and L. Fan, "Impedance Model-Based SSR Analysis for TCSC Compensated Type-3 Wind Energy Delivery Systems," *IEEE Trans. Sustainable Energy.*, vol. 6, no. 1, pp. 179–187, Jan. 2015.

[14] L. Fan, and Z. Miao, "Nyquist-Stability-Criterion-Based SSR Explanation for Type-3 Wind Generators," *IEEE Trans. Energy Convers.*, vol. 27, no. 3, pp. 807–809, Sep. 2012.

[15] L. Fan, and Z. Miao, "Mitigating SSR Using DFIG-Based Wind Generation," *IEEE Trans. Sustainable Energy.*, vol. 3, no. 3, pp. 349–358, July 2012.

[16] Y. Song, X. Wang, F. Blaabjerg, "High Frequency Resonance Damping of DFIG based Wind Power System under Weak Network," *IEEE Trans. Power Electron*., vol. pp, no. 99, early access, 2016.

[17] Y. Song, X. Wang, F. Blaabjerg, "Impedance-Based Super-Synchronous Resonance Analysis of DFIG System in Weak Grids," *IEEE Trans. Power Electron*., vol. pp, no. 99, early access, 2016.

[18] Y. Song, and F. Blaabjerg, "Wide Frequency Band Active Damping Strategy for DFIG System High Frequency Resonance," *IEEE Trans. Energy Convers.*, vol. PP, no. 99, early access, 2016.
[19] X. Wang, F. Blaabjerg, and P. C. Loh, "Grid-Current-Feedback Active Damping for LCL Resonance in Grid-Connected Voltage Source Converters," *IEEE Trans. Power Electron.*, vol. 31, no. 1, pp. 213-223, Jan. 2016.
[20] X. Wang, F. Blaabjerg, and Z. Chen, "Synthesis of Variable Harmonic Impedance in Inverter-Interfaced Distributed Generation Unit for Harmonic Damping Throughout a Distribution Network," *IEEE Trans. Ind. Appl*., vol. 48, no. 4, pp. 1407-1417, July-Aug. 2012.
[21] X. Wang, F. Blaabjerg, and Z. Chen, "Autonomous Control of Inverter Interfaced Distributed Generation Units for Harmonic Current Filtering and Resonance Damping in An Islanded Microgrid," *IEEE Trans. Ind. Appl*., vol. 50, no. 1, pp. 452-461, Jan.-Feb. 2014.
[22] X. Wang, Y. Li, F. Blaabjerg, and P. C. Loh, "Virtual-Impedance-Based Control for Voltage-Source and Current-Source Converters," *IEEE Trans. Power Electron*., vol. 30, no. 12, pp. 7019-7037, Dec. 2015.
[23] C. Bao, X. Ruan, X. Wang, W. Li, D. Pan, and K. Weng, "Step-by-Step Controller Design for LCL-Type Grid-Connected Inverter with Capacitor–Current-Feedback Active-Damping," *IEEE Trans. Power Electron*., vol. 29, no. 3, pp. 1239-1253, Mar. 2014.
[24] D. Pan, X. Ruan, C. Bao, W. Li, and X. Wang, "Optimized Controller Design for LCL-Type Grid-Connected Inverter to Achieve High Robustness Against Grid-Impedance Variation," *IEEE Trans. Ind. Electron*., vol. 62, no. 3, pp. 1537-1547, Mar. 2015.
[25] D. Pan, X. Ruan, C. Bao, W. Li, and X. Wang, "Capacitor-Current-Feedback Active Damping With Reduced Computation Delay for Improving Robustness of LCL-Type Grid-Connected Inverter," *IEEE Trans. Power Electron*., vol. 29, no. 7, pp. 3414-3427, July 2014.
[26] D. Yang, X. Ruan, and H. Wu, "A Real-Time Computation Method With Dual Sampling Mode to Improve the Current Control Performance of the LCL-Type Grid-Connected Inverter," *IEEE Trans. Ind. Electron*., vol. 62, no. 7, pp. 4563-4572, July 2015.
[27] D. Yang, X. Ruan, and H. Wu, "Impedance Shaping of the Grid-Connected Inverter with LCL Filter to Improve Its Adaptability to the Weak Grid Condition," *IEEE Trans. Power Electron*., vol. 29, no. 11, pp. 5795-5805, Nov. 2014.
[28] S. Zhang, S. Jiang, X. Lu; B. Ge, and F. Z. Peng, "Resonance issues and damping techniques for grid-connected inverters with long transmission cable," *IEEE Trans. Power Electron*., vol. 29, no. 1 pp. 110-120, Jan. 2014.
[29] X. Wang, F. Blaabjerg, and M. Liserre, "An active damper to suppress multiple resonances with unknown frequencies," *IEEE Applied Power Electronics Conference and Exposition* (*APEC*), 2014.
[30] http://se.mathworks.com/help/physmod/sps/powersys/ref/threephasepisectionline.html

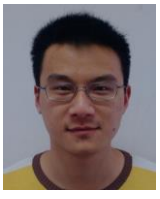

Yipeng Song (M'16) was born in Hangzhou, China. He received the B.Sc. degree and Ph.D. degree both from the College of Electrical Engineering, Zhejiang University, Hangzhou, China, in 2010 and 2015. He is currently working as a Postdoc at the Department of Energy Technology in Aalborg University, Denmark. His current research interests are motor control with power electronics devices in renewable-energy conversion, particularly the control and operation of doubly fed induction generators for wind power generation.

Frede Blaabjerg (S'86–M'88–SM'97–F'03) was with ABB-Scandia, Randers, Denmark, from 1987 to 1988. From 1988 to 1992, he was a Ph.D. Student with Aalborg University, Aalborg, Denmark. He became an Assistant Professor in 1992, Associate Professor in 1996, and Full Professor of power electronics and drives in 1998. His current research interests include power electronics and its applications such as in wind turbines, PV systems, reliability, harmonics and adjustable speed drives.

He has received 17 IEEE Prize Paper Awards, the IEEE PELS Distinguished Service Award in 2009, the EPE-PEMC Council Award in 2010, the IEEE William E. Newell Power Electronics Award 2014 and the Villum Kann Rasmussen Research Award 2014. He was an Editor-in-Chief of the IEEE TRANSACTIONS ON POWER ELECTRONICS from 2006 to 2012. He is nominated in 2014 and 2015 by Thomson Reuters to be between the most 250 cited researchers in Engineering in the world.

Xiongfei Wang (S'10-M'13) received the B.S. degree from Yanshan University, Qinhuangdao, China, in 2006, the M.S. degree from Harbin Institute of Technology, Harbin, China, in 2008, both in electrical engineering, and the Ph.D. degree from Aalborg University, Aalborg, Denmark, in 2013. Since 2009, he has been with the Aalborg University, Aalborg, Denmark, where he is currently an Assistant Professor in the Department of Energy Technology. His research interests include modeling and control of grid-connected converters, harmonics analysis and control, passive and active filters, stability of power electronic based power systems.

He received an IEEE Power Electronics Transactions Prize Paper award in 2014. He serves as the Associate Editor of IEEE TRANSACTIONS ON INDUSTRY APPLICATIONS and the Guest Associate Editor of IEEE JOURNAL OF EMERGING AND SELECTED TOPICS IN POWER ELECTRONICS Special Issue on Distributed Generation.